CHAPTER-6

STUDIES ON $Bi_{25}FeO_{40}$ CERAMIC

6.1. Introduction

1. Introduction:

In modern technology, the bismuth ferrite has been widely used in various applications by possessing the desirable magnetic and high photocalytic activity.[1] There are several research are ongoing on the toxicity of the photo-catalysts in present time because they are developing the most serious environmental problems[2]. Although, TiO_2 is more effective photo catalyst, keeps low visible-light-response capability owing to its wide band-gap (Eg=3.2 eV) [3,4]· TiO_2 nanoparticale are also used for purifying of drinking water as reported earlier [5]. Introduction of Nd^{+3} dopent in the TiO_2 does not singnificantly impact on the magnetic properties of $NiFe_2O_4$ core which facilitates removal of the composite parricles from their surface that is why they permit their removal from the sprayed surface. Therefore, substitution of Nd+3 in the titania-coated nickel ferrite composite nanoparticles considerably improves the photocatalytic degradation of methyl orange and the anti-microbial performance [6]. Recently, bismuth ferrites have been found more attention as visible-light sensitive photocatalysts Furthermore, Sellenite materials having the general formula $Bi_{25}MO_{20 \pm \delta}$ (where M=Fe, Pb, Ni, Al) with cubic type structure (space group-123), a member of bismuth ferrites are more effective photo- catalyst due to possession of smaller band gap (Eg=1.8 eV). . These materials recently develop the great interests for the promising in optical and electrical applications [7,8] On the other hand, TiO_2 possess lesser photo-catalytic efficiency and higher band gap energy than the $Bi_{25}FeO_{40}$ because TiO_2 absorbs only 3~4% ultraviolet light in the whole visible-light content (47%) of the solar spectra [9,10]. Generally, bismuth ferrites are three type such as $Bi_{25}FeO_{40}$, $Bi_2Fe_4O_9$ and $BiFeO_3$ in which $Bi_{25}FeO_{40}$ exhibits in sillenite type of structure, $Bi_2Fe_4O_9$ are multiferroic materials with orthorhombic structure $BiFeO_3$ are the perovskite type material. Out of which, Sillenite materials are newly drawn much attention because of their physical properties and technological applications in sensing, actuation, and digital memory [3,7,11,12]. Sillenite materials $Bi_{25}FeO_{40}$ with special Bi–O polyhedron structure, shows the promising properties such as high piezo modulus, high carrier mobility and high photo-sensitivity [13,14], implying the potential application in piezotechnics, acoustics and piezotechnics. $BiFeO_3$ having a rhombohedrally distorted perovskite structure is one of the well-known perovskite possessing multiferroic behaviors. Mullite-type $Bi_2Fe_4O_9$ is an important functional compound which has been recommended as an effective non-platinum catalyst due to high catalytic effectiveness for ammonia oxidation to NO. Some nanocrystalline ferrite also used as a magnetic carrier for drug delivery[15] and also used as removal antimicrobial photocatalyst composite nanoparticles [16,17] Single crystals of $Bi_{25}FeO_{40}$ were produced by top seeded solution growth technique[18]. M. Valant [19] proposed that the structural formula of iron sillenite is $Bi_{12}(Bi_{1/2}Fe_{1/2})O_{19.5}$ and Bi^{5+} ions do not exist in the structure, but in $Bi_{25}FeO_{40}$, Bi^{+5} exists in the structure iron sillenite, 24 Bi^{+3} and one Bi^{+5}exists . Recently, semiconductor photocatalytic technology has been considered as an effective approach for the decrease of aqueous pollutants in waste water and great expectation in solving energy and pollution problems. In the sillenite structure of $Bi_{25}FeO_{40}$ the Bi^{+3} ion occupy the octahedral position forming a case of corner concerted BiO_5 polyhedra (E= inert $6s^2$ electron pair) whereas Bi^{+5} and Fe^{+3}ion are shearing the tetrahedral position within the cage and suggest that the Bi^{+3} tetrahedral position accompanied by oxygen vacancies. Some nanocrystalline ferrite used as a magnetic carrier for drug delivery [15] and also used as removal antimicrobial photocatalyst composite nanoparticles [20].

Now days, several low-cost and environmental adsorbents containing natural inorganic and agricultural materials have been reported for the removal of dyes from aqueous solutions[11,21] . In the present work, the synthesis and adsorption studies on $Bi_{25}FeO_{40}$ has been done and it will be an efficient and interesting method in pollutants removal due to its low-cost, great efficiency, and easy design [22]. Considering the above point, the present work is also focused to application of $Bi_{25}FeO_{40}$ as adsorbent for the removal of Methylene blue in bench scale mode under optimum operating condition.

6.2 Experimental

a ***Material Synthesis***

$Bi_{25}FeO_{40}$ (BFO) polycrystalline ceramic was synthesized by semi-wet method at sintering temperature 860 °C for 8h. The primary chemicals used for the synthesis of BFO ceramic are Bi $(NO_3)_3$ $.5H_2O$ (99 % Merck), Fe $(NO_3)_3.9H_2O$ (99% Merck) and glycine (99% Merck). In the present method of synthesis, stoichiometric ratio of Bi $(NO_3)_3.5H_2O$ and Fe $(NO_3)_3.9H_2O$ were dissolved in distilled water. Then the aqueous solution of glycine was added as per equivalent of metal ions in to the prepared mixture. The obtained mixture was heated at 70-80 °C with continuous stirring with the help of hot plate magnetic stirrer until the formation of gel by evaporation of water and nitrogen in form of their oxides. The resulting gel was burned with sooty flame because of glycine which acts as organic fuel and plays an important role during ignition step. The obtained fluffy solid mass was converted into fine powder with the help of agate and mortar. Further, procured dry powders was calcined at 700 °C for 7h and make a cylindrical pellets with the mixing of PVA binder on applying pressure of 5-6 tons by using hydraulic press. The obtained pellets were sintered at 860 °C for 8h and polished with emery paper to get a smooth surface after sintered pellets. Then, silver paste was done on both the side of pellets to make its surface conducting and carried out for dielectric and electrical measurements.

Methylene Blue (MB) ($C_{16}H_{18}ClN_3S\cdot 2H_2O$) was selected as the model dye for adsorption study of $Bi_{25}FeO_{40}$. MB stock solutions 500 mg/L was prepared by dissolving MB dye in double distill water. The experimental solutions were prepared by diluting the MB stock solutions in precise proportions to different initial concentrations. The pH of the solutions were maintained by adding 0.1N HCl and/or 0.1N NaOH. The samples were taken at regular interval and followed by centrifugation at 8000 rpm for 10 min. The optical density (O.D) of supernatant was measured by a UV-Vis spectrophotometer (ELICO SL 210, India) at 665 nm wavelength. Batch adsorption experiments were performed into Erlenmeyer flask of 250 mL. To obtain the maximum adsorption by $Bi_{25}FeO_{40}$ the process variable such as pH (4.0–11.0), adsorbent dosage (0.2–1.0 g/L), process time (0-40 min), and concentration of solution were optimized. Further, the experiments were performed at optimum process conditions. The removal efficiency (RE) and adsorption capacity (q_e (mg/g)) of $Bi_{25}FeO_{40}$ were calculated by following equations [23].

$$RE = \frac{C_o - C_t}{C_o} \times 100 \qquad (1)$$

$$q_e = \frac{(C_o - C_t)}{m} \times V \qquad (2)$$

Where, C_o and C_t, represent the initial MB concentration and concentration at time t, respectively. q_e, m and V show the adsorption capacity (mg/g), weight of adsorbent (g), and volume of MB solution (L), respectively. All the experiments were performed in triplicate.

b Material characterization

The crystalline phase of sintered material was identified by an X-rays Diffractometer (Rigakuminiflex 600, Japan) at a scan rate of 3°/min in 2θ range of 20-80° employing CuK$_\alpha$ radiation of wavelength, λ=1.54059 Å. The morphology of the fractured surface of sintered BFO was characterized by scanning electron microscope (ZEISS, model EVO–18 research; Germany).The Bright field TEM images were obtained with the help transmission electron microscopy (TEM, FEI Tecnai-20G^2) with an accelerating voltage of 200kV. For dielectric measurements, the pellets were polished and painted by silver paste; then dried at 300 °C for 3h to form electrodes for the respective characterizations. Electrical measurement data were taken by LCR meter (PSM1735-NumtriQ, Nuwton 4th Ltd Uk) by varying the temperature and frequency.

6.3 Results and Discussion

X-ray diffraction pattern of $Bi_{25}FeO_{40}$ (BFO) polycrystalline ceramic sintered at 800 °C for 8 h is shown in Fig. 1 which clearly depict the single phase formation of

$Bi_{25}FeO_{40}$ and no secondary phase are detected in the material and well matched with JCPDS card no. 46-0416. The most intense peaks of BFO ceramic corresponding to the planes (310), (220), (530), (222), (600), (611), (631), (332) are observed in the XRD pattern. All the characteristic peaks of XRD data were indexed on the basis of a cubic unit cell similar to $Bi_{25}FeO_{40}$. The lattice parameter and unit cell volume of BFO ceramic were determined by using "Cel" software having lattice parameter a=1.01897 nm. The crystallite size (D) of BFO ceramic was calculated with the help of Debye–Scherer's formula.

$$D= k\lambda/\beta \cos \theta \qquad (3)$$

where, K is a dimensionless shape factor, with a value taken as 0.90, λ is the wavelength of X-ray, θ is the diffraction angle (Bragg angle), and β is the line broadening at half the maximum is the peak width of the diffraction peak at half-maxima (FWHM) in radians. The β is corrected value of diffraction peak due to instrumental broadening for crystallite size 13.6 nm with reference to standard silicon wafer sample.

6.3.1. Microstructural studies

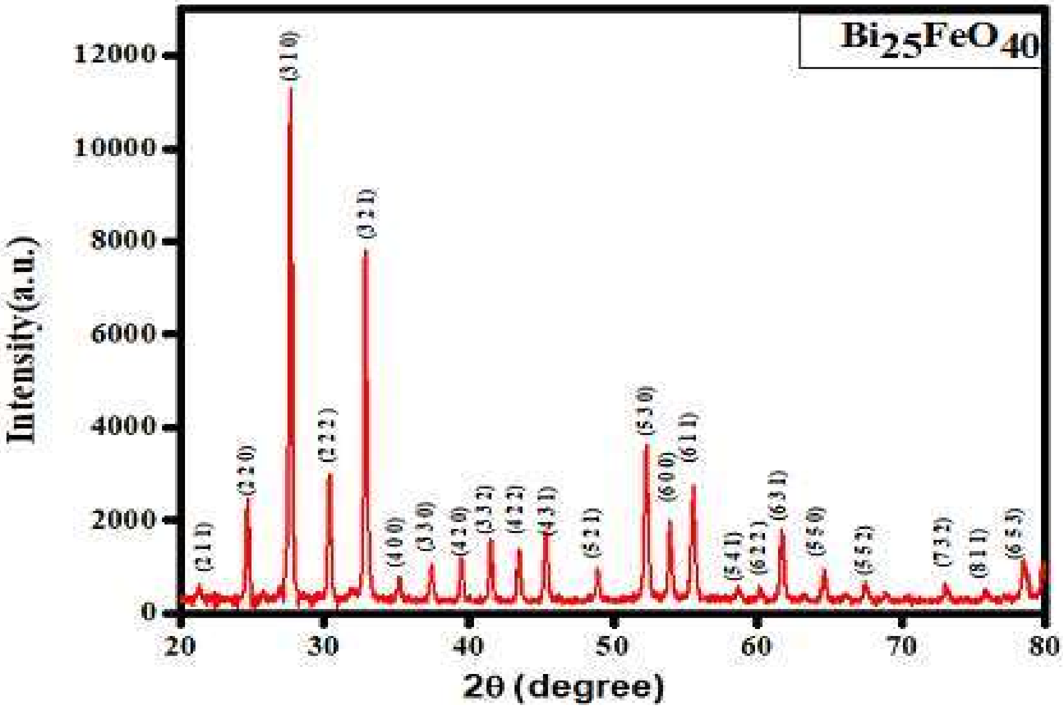

Fig 6.1. X-ray diffraction (XRD) pattern of $Bi_{25}FeO_{40}$ (BFO) ceramic sintered at 800°C for 8 h.

In order to confirm the valence state of the elements in the $Bi_{25}FeO_{40}$, XPS analyses were carried out and given in Fig 2. Figure 2 (a) shows a wide-scan XPS spectrum of Bismuth, in which two peaks are observed at 158.8 eV and 164.04 eV binding energies respectively. Peak assigned at 158 and 164 eV binding energy are due to presents of two valance state $Bi^{+3,}$ ($4f_{7/2}$) and Bi^{+5}($4f_{5/2}$) respectively in the $Bi_{25}FeO_{40}$ ceramic. ($24Bi^{+3}$, one Bi^{+5} a having binding energy).

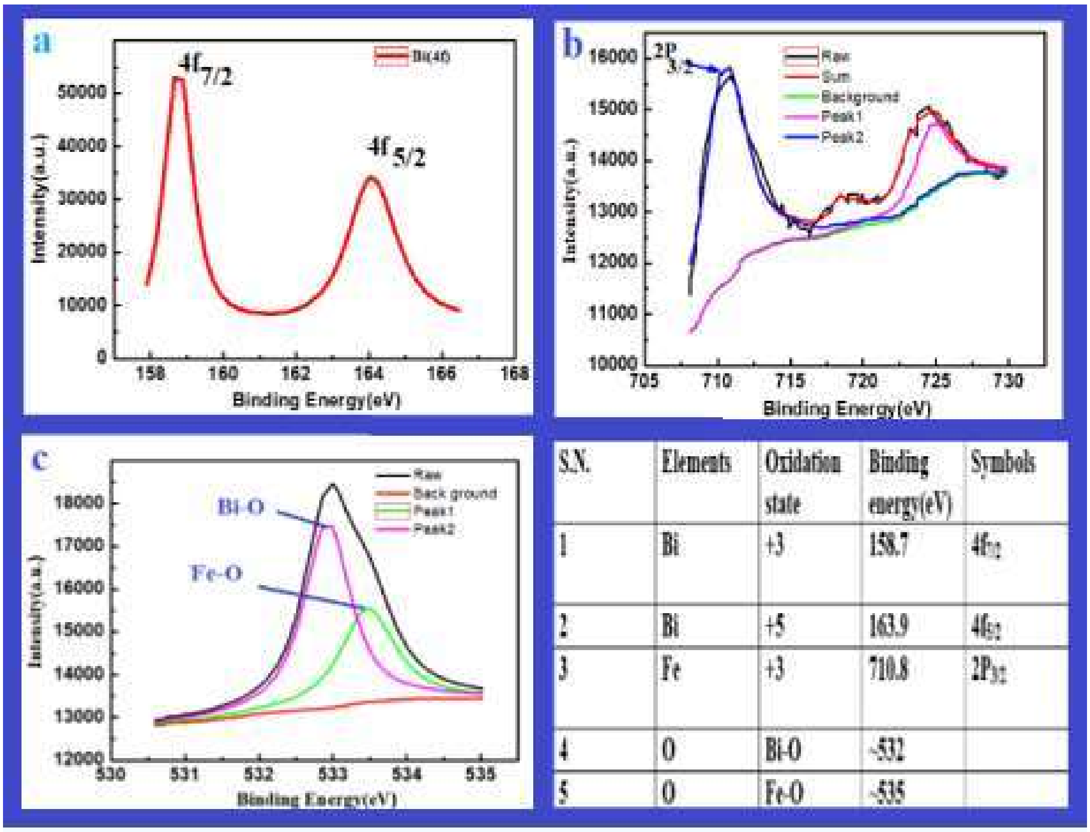

S.N.	Elements	Oxidation state	Binding energy(eV)	Symbols
1	Bi	+3	158.7	$4f_{7/2}$
2	Bi	+5	163.9	$4f_{5/2}$
3	Fe	+3	710.8	$2P_{3/2}$
4	O	Bi-O	~532	
5	O	Fe-O	~535	

Fig 6.2. XPS spectra of (a) Bi (b) Fe and (c) Oxygen for BFO sample sintered at 800°C for 8 h.

Figure 2 (b) shows the Fe 2p spectra doublet consist of two peaks of Fe $2p_{3/2}$ (710.8 eV) and Fe $2p_{1/2}$ (724.6 eV), which corresponding to the characteristics of Fe^{3+} ions. In Fig. 2(c), the peak of O 1s at 532.1 eV and 533.5 eV can be assigned to the binding energies of O in the Fe–O and Bi–O chemical bonds, respectively[24–27].

Fourier transforms infrared (FTIR) spectra of the $Bi_{25}FeO_{40}$ before and after adsorption was recorded in the wavelength range of 509.6-1712 cm^{-1} is shown in Fig. 3.

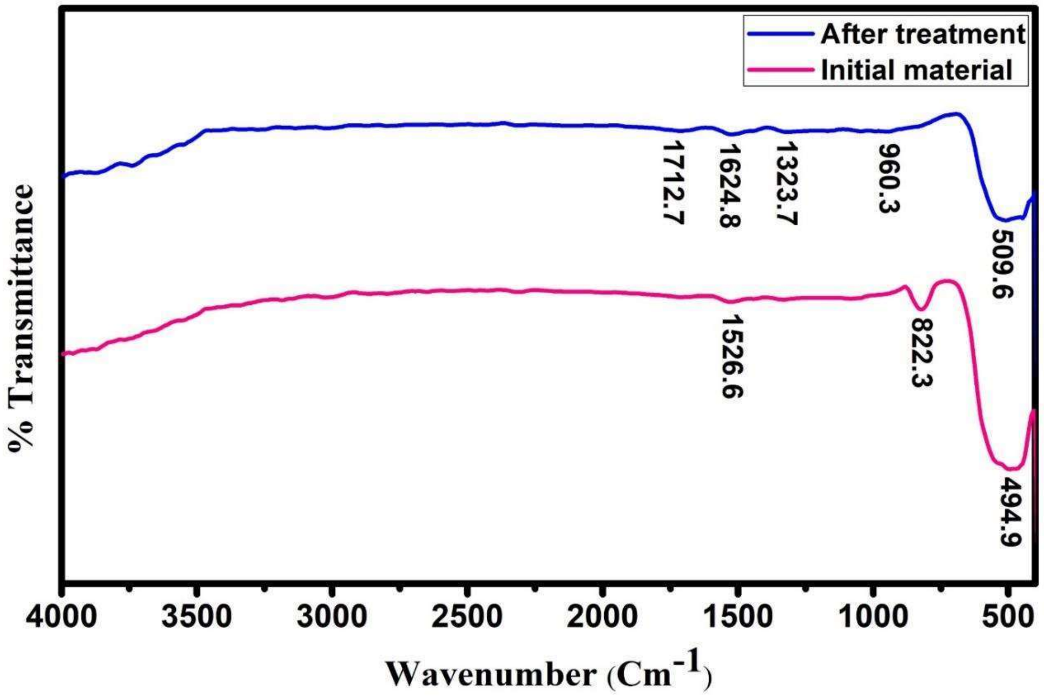

Fig 6. 3. FTIR spectra of $Bi_{25}FeO_{40}$ (BFO) ceramic before adsorption and after treatment of adsorption.

Some functional group is present in the FTIR spectra before adsorption, but additional functional group are appeared in the $Bi_{25}FeO_{40}$ after adsorption. Presence of these additional groups after adsorption may be due to adsorption of methylene blue on the surface of BFO sample.

The bright field TEM image of $Bi_{25}FeO_{40}$ polycrystalline ceramic before and after dye (M.B) adsorption is shown in Fig. 4 (a) and (b) exhibit cubic nature of the particles. The average particle size calculated by using Image j software and found to be 50.0864 nm.

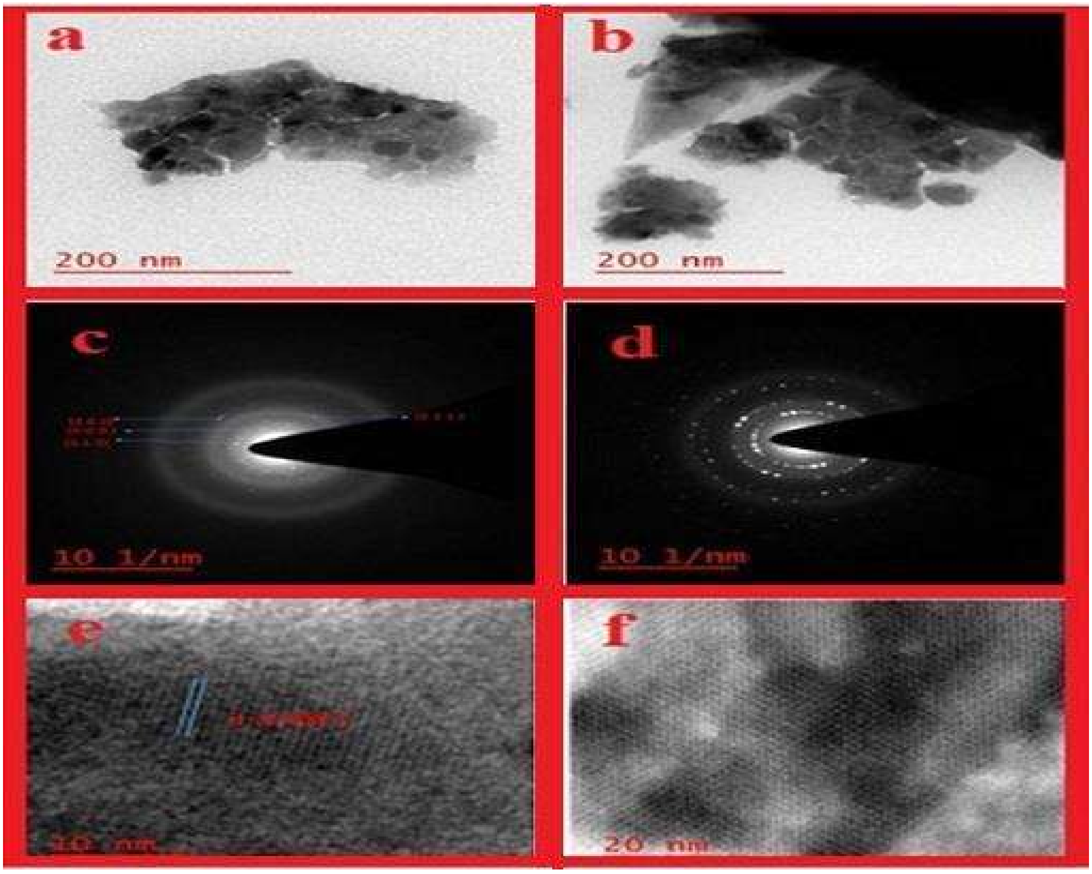

Fig 6.4(a) and (b) represent bright field TEM image (c) and (d) indicate SAED pattern (e) and (f) HR -TEM images of BFO ceramic before and after adsorption.

Selected area diffraction (SAED) pattern is mentioned in Fig. 4 (c) and (d) which reveals the more crystalline in nature after MB adsorption than without adsorption. Figure 4 (e) and (f) show high resolution HR-TEM images which exhibits the presence of some fringes with d-spacing 0.988 Å in case of without adsorption which are good agreements with XRD pattern (JCPDS cord number: 46-0416), whereas the agglomeration of fringes and formation of layer occurs due to MB adsorption on the surface of the $Bi_{25}FeO_{40}$ and some dye molecule also filler in to the force.

6.3. Before and After Adsorption Treatment of SEM image

SEM images of $Bi_{25}FeO_{40}$ (BFO) polycrystalline ceramic before and after dye (M.B) adsorption sintered at 860 °C for 8 h is shown in Fig. 5 (a) and (b). SEM shows the clear appearance of grains with cubical structure before adsorption and porosity is also found in the materials, whereas agglomeration of the particle with higher grain size occurred after treatment of adsorption.

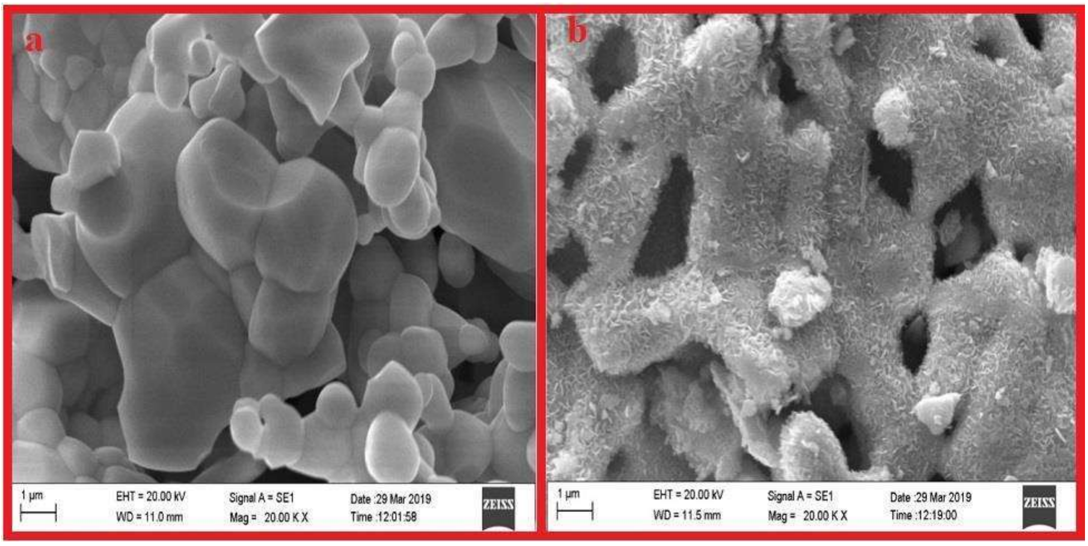

Fig. 6.5 SEM images of $Bi_{25}FeO_{40}$ (BFO) ceramic (a) before treatments with methylene blue, (b) after treatments with methylene blue.

The average grain size of the $Bi_{25}FeO_{40}$ ceramic calculated with the help of image J software before adsorption is found to be 2.57 µm which is lower than the size of grain 3.45 µm obtained after treatment of adsorption.

6.4. Adsorption Studies:

a. Effect of contact time

The adsorption of the MB solution into $Bi_{25}FeO_{40}$ is widely depending on the contact time. Fig. 6 exhibits the effect of contact time on MB removal (%) at different concentration of MB. Initially, MB removal was very fast and reached to equilibrium after a very short contact time. For 10 mg/L of initial MB concentration, 91.3% of removal was obtained at 15 min of contact time and reached to equilibrium with 95.23% removal at 30 min. Similar effects were observed for 20, 30, 40, and 50 mg/L of MB solution. From obtained results, a contact time of 30 min was applied for all adsorption experiments. Furthermore, it can be observed from figure that removal efficiency were decreasing with increasing of initial MB concentration.

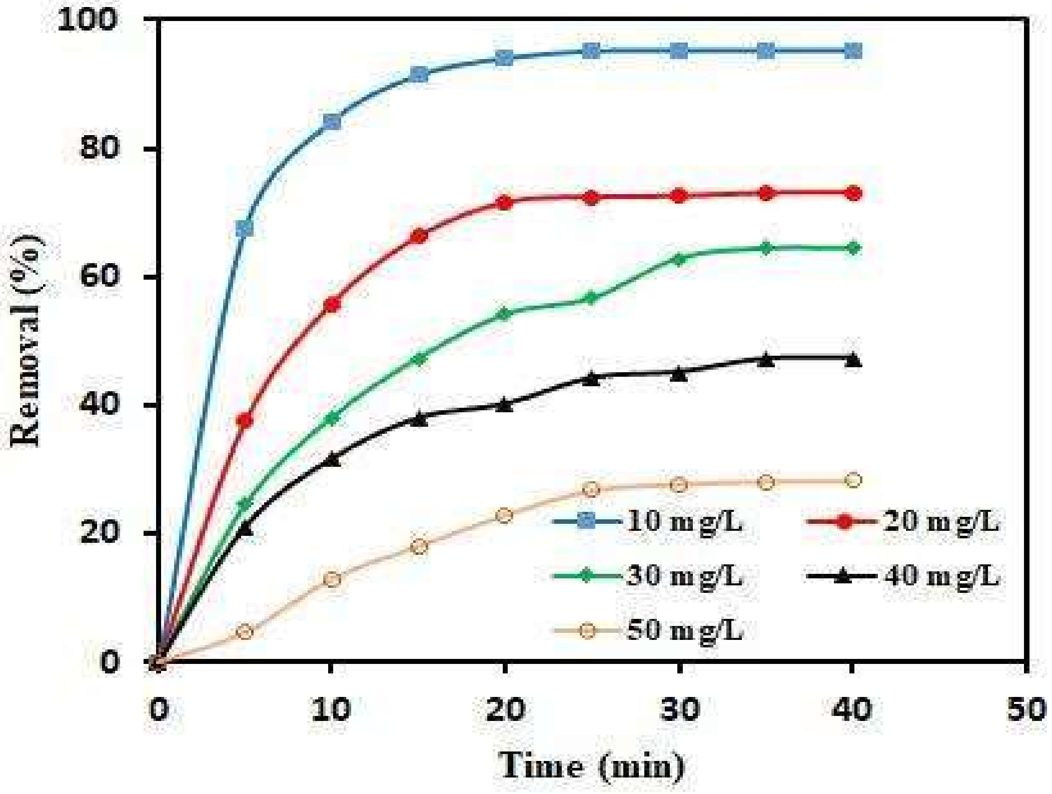

Fig. 6.6. The effect of contact time on MB removal (%) at different concentration of MB.

The highest removal efficiency (95.2%) was obtained at 10 mg/L of MB concentration, while the lowest removal efficiency was observed at 50 mg/L. The decreased in the removal efficiency with increasing MB concentration may be due to competition for the active sites on the adsorbents at higher MB concentration. According to [28], competition of dye molecules on adsorbent surface lead to saturation of active sites and responsible for decline in removal and adsorption efficiency[23] studied the effect on MB concentration (4-40 mg/L) on adsorption efficiency. It observed that as increased in MB concentration, the adsorption capacity was decline.

b Effect of Adsorbent Dose

Figure 7 shows the effect of adsorbent dose (0.2-1.0 g/L) on the removal (%) of MB. Initially, rapid removal of MB was observed due to more availability surface area for adsorption. As increased in adsorbent dose, the removal rate becomes very rapid. At adsorbent dose of 0.2 g/L, 52.5 % removal was obtained while 96.1 % of removal was observed at 0.8 g/L of adsorbent at 20 ppm of MB with 30 min of contact time. The removal efficiency was not significantly enhance by increasing the adsorbent dose of above 0.8 mg/L.

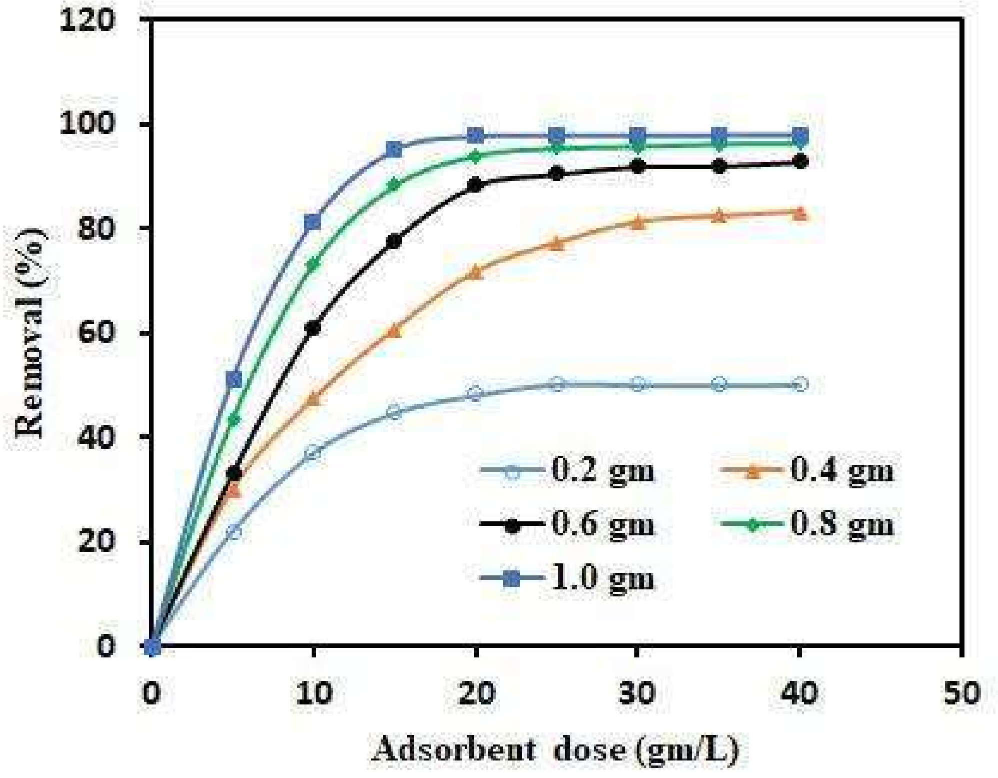

Fig 6.7. Effect of adsorbent dose (0.2-1.0 g/L) on the removal (%) of MB.

This may be due to all MB was adsorbed into active sites of the adsorbent and any increase in adsorbent dosage did not yield a higher MB uptake [29]. Thus, an optimal dosage of adsorbent was found to be 0.8 g/l for maximum removal of MB shows the similar effect of adsorbent dose on removal efficiency. [30]

c Effect of pH

Electrostatic interaction between adsorbent and adsorbate is effected by change in pH of the solution and consequently affected the surface charge of the adsorbent. Due to cationic nature of MB, at acidic medium, solution provide more positive charge to surface of adsorbent by introducing H^+ ions. These H^+ ions will lead the electrostatic repulsion between MB and adsorbent, which followed by decline in the adsorption capacity of adsorbent [31].

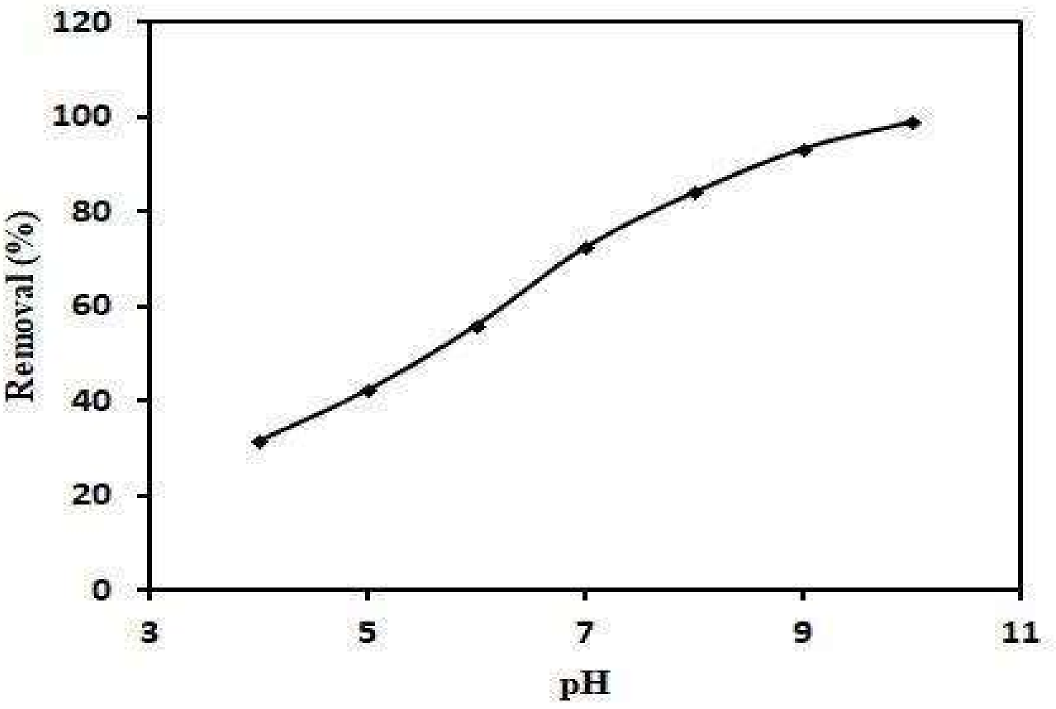

Fig 6. 8. The effect of pH (4.0-10.0) on removal efficiency of MB.

At alkaline condition, the surface of adsorbent become more negatively charged, which leads to an electrostatic attraction between MB and adsorbent surface. Figure 5.8 shows the effect of pH (4.0-10.0) on removal efficiency of MB. The lower removal efficiency (31.41%) was observed at 4.0 pH. Further, as increased in the pH, the removal efficiency of MB was increased. The maximum removal of 98.3% was obtained at 10.0 pH. This may due to surface of adsorbent become more negatively charged at higher pH which gradually enhanced the electrostatic attraction between MB and adsorbent.

d. Equilibrium adsorption isotherm studies

An adsorption isotherm reveals the equilibrium between adsorbent and adsorbate. Several isotherm models have been developed to study the modelling of adsorption process.

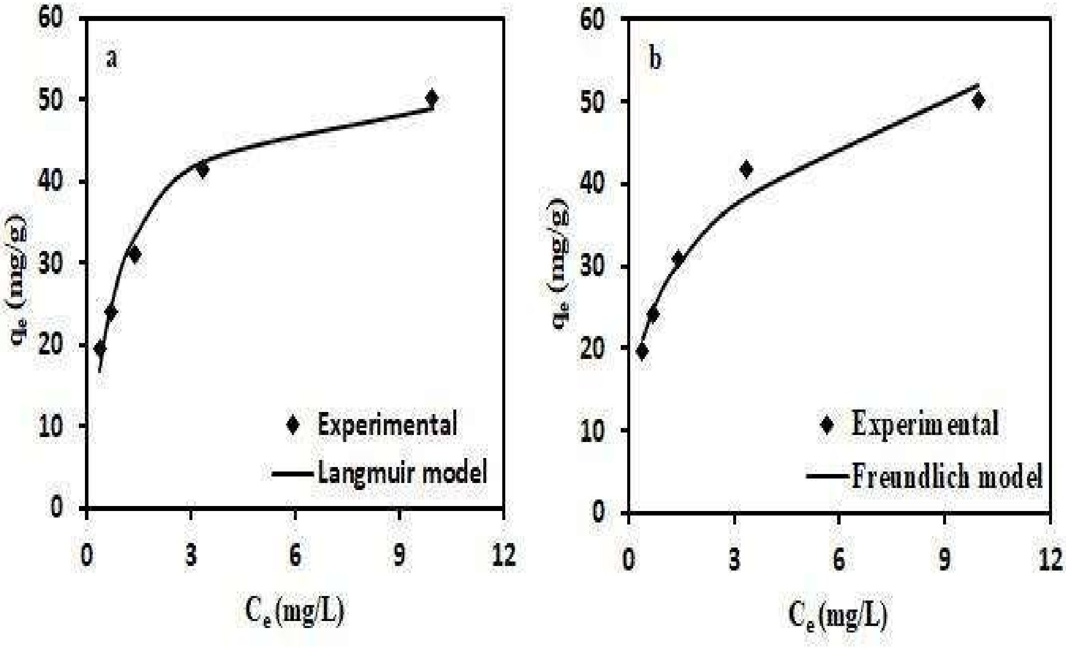

Fig 6 .9. The adsorption isotherms of MB by $Bi_{25}FeO_{40}$ samples; the data from experiment have been fitted by Langmuir and Freundlich isotherm models.

Langmuir and Freundlich isotherm models were widely used to describe the interaction between adsorbate molecules and adsorbent surface.[21]

e Freundlich isotherm

The Freundlich isotherm model is applied to study the adsorption performance on the heterogeneous system.[23] Freundlich isotherm model is represented below as non-linear equation:

$$q_e = K_F C_e^{\frac{1}{n}} \tag{4}$$

where, q_e, C_e, and K_F represent the equilibrium adsorption capacity of adsorbent (mg/g), concentration of MB at equilibrium (mg/L), and adsorption equilibrium constant of Freundlich isotherm ((mg/g) $(L/mg)^{1/n}$), respectively. n is the Freundlich constant give the indication of how adsorption process is favorable. When $0 < 1/n < 1$, the adsorption is favorable; when the value of $1/n$ beyond 1, the adsorption is unfavorable; when $1/n = 1$, indicating the adsorption is homogeneous.[32]

g Langmuir isotherm

The Langmuir isotherm assumes that the adsorption active sites distribute homogeneously over the surface of adsorbent. Langmuir isotherm model is represented below as non-linear equation:[33]

$$q_e = \frac{q_m K_L C_e}{1 + K_L C_e} \tag{5}$$

where, q_m, and K_L represent the maximum adsorption capacity of adsorbent (mg/g), and Langmuir isotherm constant (L/mg), respectively. Figure 9 (a) and 9 (b) show the fitted curves of Langmuir and Freundlich isotherms, respectively. It was observed that the experiment data was better fitted with Langmuir isotherm models than Freundlich isotherm models, as the coefficient of determination (R^2) is higher for Langmuir isotherm. The summary of kinetic parameters has been given in Table 1.

Table 1: Kinetic parameters for the adsorption of MB onto $Bi_{25}FeO_{40}$ at 20 mg/L.

Pseudo-first order			Pseudo-second order		
q_e(mg/g)	K_1 (min^{-1})	R^2	q_e(mg/g)	K_2 (g/mg.min)	R^2
34.21	0.271	0.935	43.39	0.0041	0.989

h Kinetic studies

The kinetics of MB removal by adsorption process has been widely fitted to pseudo-first-order, pseudo-second-order. To study the adsorption kinetic, set of batch experiments were performed at different initial concentrations of MB at pH 8.0, dose of 0.8 g/L and 40 min of contact time. The adsorption kinetic of the MB onto $Bi_{25}FeO_{40}$ was evaluated by Lagrange proposed pseudo-first-order kinetic model:

$$q_t = q_e\left(1 - e^{k_1 t}\right) \tag{6}$$

Where, q_e and q_t are the adsorption capacities at equilibrium and at time t (mg/g), respectively, and k_1 is the pseudo-first-order rate constant (min^{-1}).

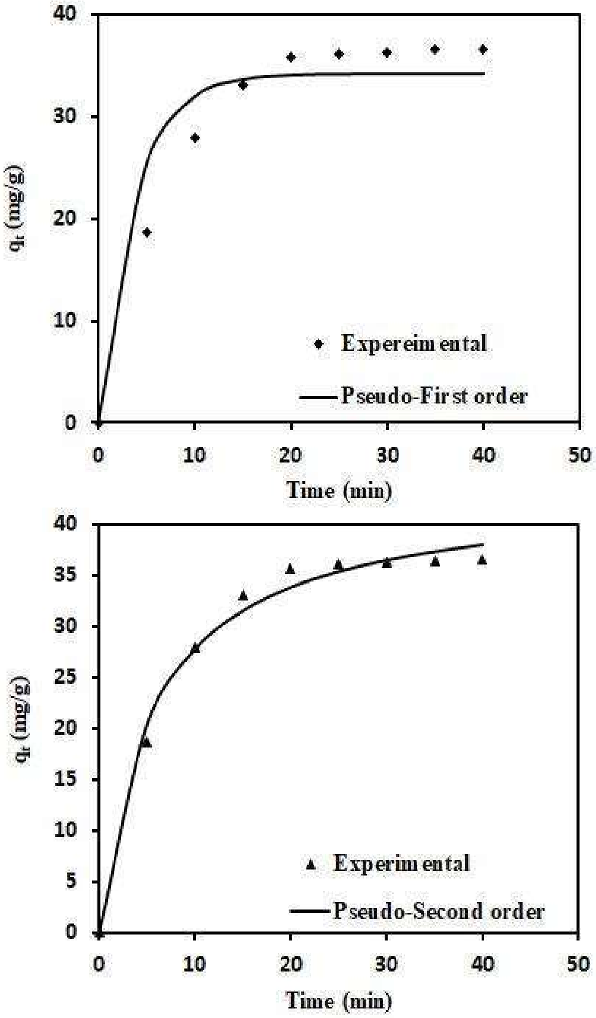

Fig 6.10 The fitted kinetics models from experiment data: (a) pseudo-first-order and (b) pseudo-second-order models, respectively.

Figure 6.10 (a) shows the fitted experimental data with pseudo-first-order model and kinetic parameters were obtained as q_e: 34.21 (mg/g) and k_1:0.271 (min^{-1}) with 0.93 of correlation coefficient (R^2), are mentioned in Table 2.

The kinetics of MB removal by adsorption process were also evaluated by the pseudo-second order kinetic model:

$$q_t = \frac{k_2 {q_e}^2 t}{1 + k_2 q_e t} \tag{7}$$

k_1 is the pseudo-second-order rate constant (g/mg.min). Figure 3(b) shows the fitted experimental data with pseudo-first-order model. The kinetic parameters; *qe* and k_2 were found to be 43.39 (mg/g) and 0.0041 (g/mg. min), respectively with 0.98 of correlation coefficient (R^2) are also shown in Table 2.

Table 2: Parameters of adsorption isotherms for MB onto $Bi_{25}FeO_40$`.

Freundlich model			Langmuir model		
K_F[(mg/g)(L/mg)$^{1/n}$]	*1/n*	R^2	q_e(mg/g)	K_L(L/mg)	R^2
27.52	0.276	0.97	53.12	1.182	0.98

6.6 Electrical studies:

In the sillenite material depending on how well known the conducting behavior in these materials are, it is possible to gain an in-depth understanding of their photoconductivity and optical activity, thus help in the optimization of their Properties.

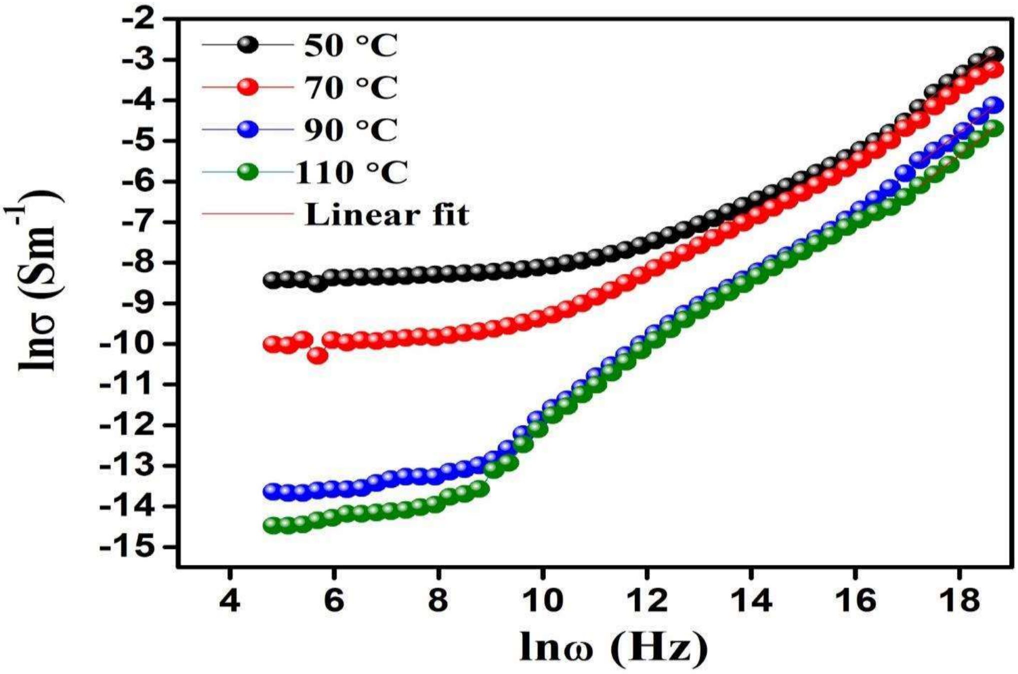

Fig 6.11. Variation of electrical conductivity with frequency at few selected temperatures of BFO ceramic sintered at 800°C for 8 h

Figure 11 displayed the frequency dependent conductivity behavior at different temperature. The electrical transport properties of the materials derived from AC conductivity and calculated with the help of Jonscher's power law

$$\sigma_{AC} = \sigma_{DC} + A\omega^{s} \tag{8}$$

where, σ_{DC} is the frequency independent conductivity dominant at the lower frequency region, A is the temperature dependent pre-exponential factor and s is the exponent parameter (0>s>1), dependent on both of materials and temperature and frequency independent. The value of frequency exponent parameter (s) calculated from the slope of the plot (ln σ vs. ln ω) for $B_{25}FeO_{40}$ ceramic and found to be 0.9119, 0.3232, 0.97453 and1.0043 at 323, 343, 363 and 483 K respectively. It is observed that the obtained value of s decreases with increasing temperature which justifies hopping charge mechanism given by Elliot for crystalline oxide materials.

Figure 13 shows the temperature - dependent conductivity at different frequencies. It reveals from figure that conductivity increases with increase in temperature, which suggests that at lower temperature region DC conductivity predominant over AC conductivity because σac considerably depends on the frequency. As temperature increases dielectric relaxation takes place, which reduces the frequency dependence of AC conductivity.

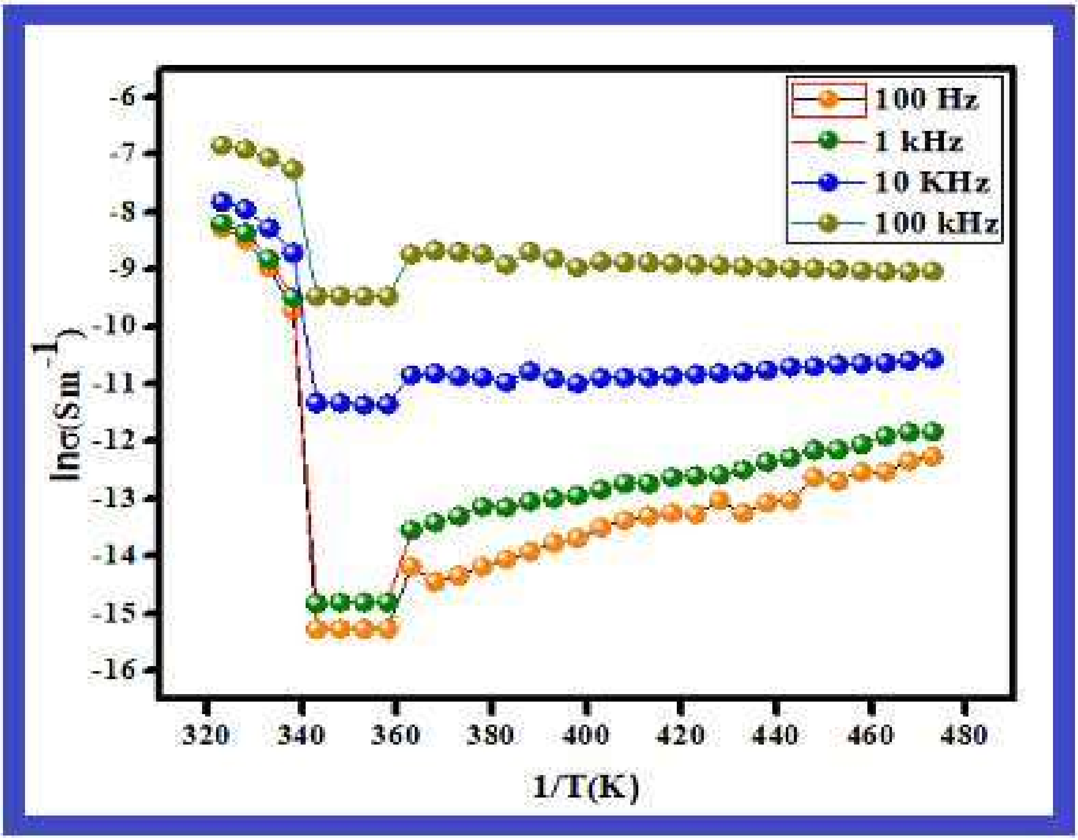

Fig 6.12. Variation of electrical conductivity with Temperature at few selected temperatures of BFO ceramic sintered at 800°C for 8 h

Therefore, conductivity mainly depends on temperature. According to Arrhenius law, temperature dependent conductivity (σ) expressed by the following equation

$$\sigma = \sigma_0 e - Ea/kT \qquad (9)$$

where, E_a is the activation energy for ionic conduction, σ_0 pre-exponential factor k is the Boltzmann constant, and T is the absolute temperature. At higher temperature, AC and DC remains same due to curves are merge to each and onset of intrinsic conductivity take place. At lower temperature region the activation energy (E_a) of $Bi_{25}FeO_{40}$ ceramic are found to be 0.50, 0.48, 0.45 and 0.29 eV at 100 Hz, 1 kHz, 10 kHz, and 100 kHz respectively. It is observed that the value of activation energy (E_a)

decrease with increasing frequency. The above mentioned results displayed the good conducting behavior of $Bi_{25}FeO_{40}$ as previously reported similar sillenite material. [34]

6.6 Conclusions:

$Bi_{25}FeO_{40}$ ceramic successfully synthesized via glycine–assisted chemical route and studied as efficient photo catalysts. The fabricated photocatalysts were characterized using different characterization techniques, such as X-ray diffraction (XRD), Fourier transform infrared (FT-IR), Scanning electron microscopy (SEM), transmission electron microscopy (TEM) and X-ray photoelectron spectroscopy (XPS). Furthermore, the photocatalytic activities of synthesized $Bi_{25}FeO_{40}$ were evaluated by photodegradation of Methylene blue dye. The process variables such pH, process time, adsorbent dose, and initial Methylene blue concentration were optimized at batch mode and the outcomes demonstrate that $Bi_{25}FeO_{40}$ shows the preeminent potential for the photodegradation Methylene blue dye. The kinetics of dye degradation were evaluated by pseudo-first and second order mechanism. Langmuir and Freundlich isotherm model were successfully applied on experimental data to estimate the adsorption phenomena. .The temperature dependent DC conductivity observed by Arrhenius equation explains the hopping charge mechanism in the BFO ceramic.

References

1 Y. Sun, X. Xiong, Z. Xia, H. Liu, Y. Zhou, M. Luo, and C. Wang, Ceram. Int. **39**, 4651 (2013).

2 R. Köferstein, T. Buttlar, and S.G. Ebbinghaus, J. Solid State Chem. **217**, 50 (2014).

3 X. Li, S. Liu, K. Lv, D. Wang, H. Zuo, J. Sun, and K. Deng, J. Hazard. Mater. **161**, 396 (2008).

4 A. Matusevich, A. Tolstik, M. Kisteneva, S. Shandarov, V. Matusevich, A. Kiessling, and R. Kowarschik, Appl. Phys. B Lasers Opt. **92**, 219 (2008).

5 C.Y. Zhang, H.J. Sun, W. Chen, J. Zhou, B. Li, and Y.B. Wang, IEEE Int. Symp. Appl. Ferroelectr. 1 (2009).

6 X. Lin, F. Huang, W. Wang, Y. Xia, Y. Wang, M. Liu, and J. Shi, Catal. Commun. **9**, 572 (2008).

7 W.F. Yao, H. Wang, X.H. Xu, J.T. Zhou, X.N. Yang, Y. Zhang, S.X. Shang, and M. Wang, Chem. Phys. Lett. **377**, 501 (2003).

8 W. Ji, K. Yao, and Y.C. Liang, Adv. Mater. **22**, 1763 (2010).

9 H. Vogt, K. Buse, H. Hesse, E. Krätzig, and R.R. García, J. Appl. Phys. **90**, 3167 (2001).

10 Z. Liu, Y. Qi, and C. Lu, J. Mater. Sci. Mater. Electron. **21**, 380 (2010).

11 S.K. Iyemperumal, T.G. Fenton, S.L. Gillingham, A.D. Carl, R.L. Grimm, G. Li, and N.A. Deskins, J. Chem. Phys. **151**, 054702 (2019).

12 M.N. Popescu, A. Domínguez, W.E. Uspal, M. Tasinkevych, and S. Dietrich, J. Chem. Phys. **151**, 067101 (2019).

13 M.T. Borowiec, A. Majchrowski, H. Szymczak, T. Zayarniuk, E. Michalski, and M. Barañski, **5136**, 26 (n.d.).

14 M. Valant and D. Suvorov, Chem. Mater. **14**, 3471 (2002).

15 B.N. Rai, J. Water Supply Res. Technol. | 1 (2018).

16 A.R. Tehrani-bagha, H. Nikkar, N.M. Mahmoodi, M. Markazi, and F.M. Menger, DES **266**, 274 (2011).

17 K. He, G. Zeng, A. Chen, Z. Huang, M. Peng, T. Huang, and G. Chen, Compos. Part B **161**, 141 (2019).

18 D.K. Verma, B. Kumar, Kavita, and R.B. Rastogi, ACS Appl. Mater. Interfaces **11**, 2418 (2019).

19 X. Wang, W. Mao, Q. Wang, Y. Zhu, Y. Min, J. Zhang, T. Yang, J. Yang, X. Li, and W. Huang, RSC Adv. **7**, 10064 (2017).

20 C.N. Tharamani, H.C. Thejaswini, and S. Sampath, Bull. Mater. Sci. **31**, 207 (2008).

21 J. Feng, D. Fan, Q. Wang, L. Ma, W. Wei, J. Xie, and J. Zhu, Colloids Surfaces A Physicochem. Eng. Asp. **520**, 743 (2017).

22 M. Auta and B.H. Hameed, Chem. Eng. J. **237**, 352 (2014).

23 L. Mouni, L. Belkhiri, J.C. Bollinger, A. Bouzaza, A. Assadi, A. Tirri, F. Dahmoune, K. Madani, and H. Remini, Appl. Clay Sci. **153**, 38 (2018).

24 D. Pathania, S. Sharma, and P. Singh, Arab. J. Chem. **10**, S1445 (2017).

25 Ravi and L.M. Pandey, Appl. Clay Sci. **169**, 102 (2019).

26 R. Yang, D. Li, A. Li, and H. Yang, Appl. Clay Sci. **151**, 20 (2018).

27 M.A. Rauf, S.B. Bukallah, F.A. Hamour, and A.S. Nasir, Chem. Eng. J. **137**, 238 (2008).

28 L. Zhang, Y. Zou, J. Song, C.L. Pan, S.D. Sheng, and C.M. Hou, RSC Adv. **6**, 26038 (2016).